EFDA–JET–PR(13)01

D. Kalupin, I. Ivanova-Stanik, I. Voitsekhovitch, J. Ferreira, D. Coster, L.L. Alves, Th. Aniel, J.F Artaud, V. Basiuk, J.P.S. Bizarro, R. Coelho, A. Czarnecka, Ph. Huynh, A. Figueiredo, J. Garcia, L. Garzotti, F. Imbeaux, F. Köchl, M.F. Nave, G. Pereverzev, O. Sauter, B.D. Scott, R. Stankiewicz, P. Strand, ITM-TF contributors and JET EFDA contributors

Numerical Analysis of JET Discharges with the European Transport Simulator

Numerical Analysis of JET Discharges with the European Transport Simulator

D. Kalupin[2,3], I. Ivanova-Stanik[4], I. Voitsekhovitch[1], J. Ferreira[5], D. Coster[7], L.L. Alves[5], Th. Aniel[6], J.F. Artaud[6], V. Basiuk[6], J.P.S. Bizarro[5], R. Coelho[5], A. Czarnecka[4], Ph. Huynh[5], A. Figueiredo[5], J. Garcia[6], L. Garzotti[1], F. Imbeaux[6], F. Köchl[8], M.F. Nave[5], G. Pereverzev, O. Sauter[9], B.D. Scott[7], R. Stankiewicz[4], P. Strand[10], ITM-TF contributors[†] and JET EFDA contributors*

JET-EFDA, Culham Science Centre, OX14 3DB, Abingdon, UK

[1]EURATOM-CCFE Fusion Association, Culham Science Centre, OX14 3DB, Abingdon, OXON, UK
[2]EFDA-CSU Garching, Boltzmannstr. 2, D-85748, Garching, Germany
[3]Institute of Energy and Climate Research – Plasma Physics, Forschungszentrum Jülich, EURATOM Association, Trilateral Euregio Cluster, D-52425 Jülich, Germany
[4]Institute of Plasma Physics and Laser Microfusion, EURATOM Association,00-908 Warsaw, Poland
[5]Associação EURATOM/IST, Instituto de Plasmas e Fusão Nuclear, Instituto Superior Técnico, Universidade Técnica de Lisboa 1049-001 Lisboa, Portugal
[6]CEA, IRFM, F-13108 Saint-Paul-lez-Durance, France.
[7]Max-Planck-Institut für Plasmaphysik, EURATOM-IPP Association, Garching, Germany
[8]Association EURATOM-ÖAW/ATI, Atominstitut, TU Wien, 1020 Vienna, Austria
[9]Ecole Polytechnique Fédérale de Lausanne (EPFL), Centre de Recherches en Physique des Plasmas, Association EURATOM-Confédération Suisse, CH-1015 Lausanne, Switzerland
[10]Department of Earth and Space Sciences, Chalmers University of Technology, EURATOM-VR Association, SE-352 96 Göteborg, Sweden
[†]See the Appendix to the paper of G. Falchetto et al., Nuclear Fusion submitted
** See annex of F. Romanelli et al, "Overview of JET Results", (24th IAEA Fusion Energy Conference, San Diego, USA (2012)).*

Preprint of Paper to be submitted for publication in
Nuclear Fusion

ABSTRACT

The "European Transport Simulator" (ETS) [1,2] is the new modular package for 1-D discharge evolution developed within the EFDA Integrated Tokamak Modelling (ITM) Task Force. It consists of precompiled physics modules combined into a workflow through standardized input/output data-structures. Ultimately, the ETS will allow for an entire discharge simulation from the start up until the current termination phase, including controllers and sub-systems. The paper presents the current status of the ETS towards this ultimate goal. It discusses the design of the workflow, and presents the first physics applications of the ETS for the analysis of JET tokamak discharges.

1. ETS WORKFLOW DESIGN

The ETS adopts a modular approach, where standalone precompiled physics modules (actors) are coupled into the workflow through standardised interfaces linked with the ITM data-structure. In view of allowing collective development of various applications, a generic-purpose Workflow Engine, KEPLER[3], was chosen by the ITM-TF. An actor under KEPLER is a modular physics component that solves a given type of physics problem, e.g. equilibrium reconstruction, computation of transport coefficients or heating profiles. The main advantage of a high level of modularity of ITM developed tools is the possibility to optimise the workflow configuration and the choice of physics modules exactly for the modelling aims, degree of sophistication required and computation time.

The numerical solver in ETS solves 1-D transport equations for poloidal flux, electron and ion temperature, ion or electron density and toroidal velocity as a function of the toroidal flux coordinate. It allows the user to choose within several numerical schemes (implicit, Crank Nicolson, or tridiagonal matrix algorithms). Thus it is possible to optimize the code performance for the particular physics problem (stiff transport model would be a typical example). Inputs to 1-D transport equations, such as the geometry (2-D equilibrium), the transport coefficients and the sources are provided by standalone modules coupled in a self consistent way to the transport solver through generalized data structures.

A schematic design of the workflow is shown in fig.1. Each box represents a set of modules that treat the same physics problem with various degrees of sophistication. A large choice of equilibrium solvers is available (BDSEQ, EMEQ [4], SPIDER [5], EQUAL [6], HELENA [7], CHEASE [8]). Transport coefficients can be used, provided by neoclassical transport (NCLASS[9], NEOWES, NEOS [10]) as well as anomalous transport modules of different complexity, from an analytical description (Bohm-GyroBohm [11], Coppi-Tang [12], ETAIGB), to a quasi-linear description (GLF23 [13] or Weiland model[14]), up to first-principle electromagnetic turbulence models (GEM code [15]) run in parallel on the HPC-FF as an integral part of the transport simulations. Sources and sinks include the contribution of electron cyclotron heating (GRAY code [16]), neutral beam injection (NEMO code [17]), radiation from impurities and Bremsstrahlung radiation, gas puffing, pellet injection and Ohmic power. The total transport coefficients or sources for each equation can also be taken from the database or can be derived as linear combination of values provided by

different individual modules. The effect of non-linear MHD modes is taken into account through neoclassical tearing mode or sawteeth modules.

2. VALIDATION AND BENCHMARKING

A substantial part of present ITM-TF activities is dedicated to the verification and validation of the developed tools and integrated workflows[18]. This is done by means of comparison with analytical results using the method of manufactured solutions[19], by self-benchmarking (reduction tests)[19], by benchmarking of modules describing the same kind of process against each-other within the same workflow (cross benchmarking) and by benchmarking of the entire workflow against existing transport codes.

The ETS was successfully benchmarked against ASTRA[4] and CRONOS[20] integrated modelling codes.

Before a module is released for productive runs within ETS workflows, it goes through the verification exercises mentioned above. A demonstration is the benchmarking of the impurity module included in ETS.

The impurity module in the ETS workflow enables the simulation of the time evolution of the impurity density for an arbitrary number of impurities for all ionisation states [21]. The transport coefficients for impurity ions are assumed to be equal to the transport coefficients for deuterium [11]. Density sources for each ionization state include ionization, recombination and charge-exchange, where rate coefficients of the relevant process are obtained from ADAS[22] data base using generic interfaces developed by the ITM-TF. Figure 2 compares the neutral tungsten rate coefficients for line radiation obtained from the ADAS data base directly with the one obtained through the ITM-TF atomic molecular neutral and surface data (AMNS) modules. The perfect agreement between the two curves means that the interpolation schemas and interfaces developed by the ITM-TF do not corrupt the original data provided by ADAS consortium.

The impurity solver used within the ETS was benchmarked against the SANCO impurity code, installed as a part of JET analysis suite of codes [23], for conditions of a low confinement mode Pulse No: 71827 in JET. Tungsten impurity (all ionization states) has been considered. Parabolic profiles for density and temperature of main ions and interpretative equilibrium provided by EFIT equilibrium reconstruction code were introduced into both codes. Boundary conditions for individual impurity ionisation states were given by the total impurity concentration at the last closed magnetic surface, assuming a coronal distribution at the corresponding ion temperature. Figure 3 compares steady state profiles of tungsten ionization states W^{31+}–W^{35+} dominating the radiative losses under considered conditions, radiative power density and ion effective ion charge, obtained with ETS and with SANCO after 1s. of time evolution. Good agreement is achieved for all quantities between the two codes.

3. PHYSICS APPLICATION RESULTS

3.1 IMPURITY MODELLING

The ETS was applied to simulate impurity transport for the conditions of JET Pulse No: 81856 (ITER like wall) with two phases of 3.5MW of auxiliary heating delivered by ICRH and NBI respectively (fig. 4) [24]. The ICRH results in a substantial increase of both, effective charge, Z_{eff}, and radiative power, P^{RAD}, compared to the NBI phase. Main plasma profiles are less affected by the choice of auxiliary heating. Figure 5 compares experimental profiles of the electron temperature and density in both phases. Some difference in temperature is observed within 0.3 of normalized minor radius, which roughly corresponds to 10% of the volume and can not explain experimentally observed difference in total radiative loss. Thus, the plasma contamination during the ICRH phase can be caused either by an increased source of impurities or by changes in their transport.

Spectroscopic measurements of Ni impurity along the vessel midplane were obtained using the SPRED (survey poor resolution extended domain) spectrometer with the routinely used 450gmm^{-1} holographic grating. This registers the VUV spectra in the wavelength range 100–1100Å. With the Be/W plasma facing components (PFC) the VUV spectrum was dominated by mid-Z metallic impurities like Ni and also contained intense W features. The determination of Ni impurity densities, based on the combination of absolutely calibrated VUV line transition intensity measurements with the Universal Transport Code (UTC) simulations is described in details in [25]. From the Ni density the radiated power due to Ni and its contribution to the bulk plasma radiated power ($P_{rad,bulk}$) was evaluated based on calculations of the Ni cooling factor presented in [26]. The time trace of the total density of Ni obtained with SPRED for the Pulse No: 81856 is shown in fig.6. The Ni concentration is up to the factor of tree higher for the ICRH phase.

ETS simulations were configured to reproduce experimental profiles of radiated power density and a value of line-averaged effective charge at selected times (ICRH phase, $t_1 = 12.2$s; and NBI phase, $t_2 = 19$s). Three impurity species (all ionization states of W, Ni and Be) have been simulated until the steady state impurity distribution is obtained. Initial profiles and boundary conditions for individual ionization states of impurity ions are obtained from coronal distribution using experimental n_e and T_e profiles and adjusting total concentration for each impurity. Total Ni concentration was taken from experiment, total W concentration was adjusted to reproduce radiative losses and Be concentration was adjusted to reproduce Z_{eff}. For the NBI phase the total boundary concentrations were selected to $n_W = 1.1\times10^{15}m^{-3}$, $n_{Be} = 1.0\times10^{15}m^{-3}$, $n_{Ni} = 2.4\times10^{15}m^{-3}$, and for the ICRH phase these values were increased to $n_W = 4.5\times10^{15}m^{-3}$, $n_{Be} = 2.2\times10^{17}m^{-3}3$, $n_{Ni} = 5.0\times10^{15}m^{-3}$. The impurity diffusion coefficients have been computed with the L-mode particle Bohm-gyroBohm transport model [11] and assumed to be equal for all impurity ions. Since the electron temperature and density in the NBI and ICRH phases are similar, computed profiles of transport coefficients are nearly the same. Figure 7 compares the radiated power from Ni obtained in ETS simulation to the one computed directly from experimental data using UTC code.

Figure 8 compares the simulated steady state profiles of radiative power density, W_{RAD}, and

effective charge with experimentally measured ones. A reasonable agreement for total radiative power density profile has been obtained for both heating phases. The core radiation is dominated by W during both, ICRH and NBI phases, with the largest contribution from W^{25}–W^{35} ionization states. The edge radiation is dominated by Ni ions, whereas Be does not contribute much to the radiative losses. Instead, plasma effective charge is mostly due to light ions, eg. Be and Ni. On the contrary to the radiated power profile, flat or slightly peaked in the centre, the effective charge profile is hollow with the maximum at the edge.

In the simulation performed above the high radiation power during ICRH phase has been obtained by increasing the boundary density for W. Another approach to increase the W concentration in the core can be an increase of the inward W convection. Another set of simulations including Be and W was performed to study the sensitivity of P_{rad} and Z_{eff} to the boundary concentration versus convective velocity of impurity particles. Starting with the NBI phase, the Be and W sources were adjusted through their boundary values to match the experimentally measured impurity concentration and radiative losses ($n_W = 8.0\times10^{14}\ m^{-3}$; $n_{Be} = 3.0\times10^{17}\ m^{-3}$) for Be and W impurity densities assuming zero impurity convective velocity (Fig.5, blue curves). Taking these results as a reference the impurity distribution during the ICRH phase has been first simulated by assuming a radially constant inward impurity convective velocity of 0.5m/s. This results in an increase of W_{RAD} and Z_{eff}, mostly at the magnetic axis, where impurities start to accumulate (Fig.9, green curves). Such WRAD profile appeared to be inconsistent with the bolometric measurements showing a rather flat profile (see fig.8) of radiative power during the ICRH phase. In addition, taking into account a small volume contribution from the plasma centre, the total radiative losses change only within a few percent compared to the factor of 2.5 measured in experiment. At the next step, the reference case has been repeated with zero convective velocity and increased (roughly by factor 3) impurity boundary densities ($n_W = 2.35\times10^{15}\ m^{-3}$; $n_{Be} = 9.1\times10^{17}\ m^{-3}$). In this case a much better agreement with measurements for WRAD profile and Zeff is obtained. These simulations indicate that an increased impurity density is a possible reason for the W accumulation during the ICRH phase of Pulse No: 81856, although the effect of a radially shaped convective velocity (not tested here) can not be excluded.

3.2 TRANSPORT-TURBULENCE COUPLED SIMULATION

Another area where the ITM-TF is developing advanced physics capabilities of the ETS simulator, compared to existing integrated modelling transport codes, is the coupling of the core transport solver to a turbulence code, providing transport coefficients.

Recently, the electromagnetic gyrofluid turbulence code GEM [16] was coupled to the ETS workflow, as one of the possible modules to compute the anomalous transport coefficients. GEM is run remotely on HPC-FF on 256 cores while the main part of the workflow, which is serial, is run on the ITM computing cluster. Figure 8 presents the electron density and temperature profiles time evolution obtained for the conditions of the JET Pulse No: 71827, starting from the experimental

profiles at the time 12s, obtained using GEM calculated transport coefficients for the density and the temperature. It is to be noted that this is a proof of principle, as the run lasted 10 τ_{GB} whereas fully saturated turbulence requires much longer runs. GEM and ETS use different time and radial scales. GEM is implemented as a chain of 8 flux tubes, from 0 to 7, with the i-th case at normalised toroidal flux radius [(2i+1)/16]^0.7. Each flux tube takes parameters from its profile location, runs for 10 gyro-Bohm times, $\tau_{GB} = -(c_s \cdot d \ln T_e/d\rho)^{-1}$, and returns transport coefficients. Each case has a different τ_{GB} with saturation occurring on a scale of about $100 \cdot \tau_{GB}$. The updated transport coefficients are used by ETS on its own (transport) time scale. The time within GEM is used merely to control evolving saturation. A fully relaxed run under ETS should take between 100 and 1000 loop steps, depending on proximity to instability thresholds and pathologies which can occur there. Obtaining fully saturated runs is work in progress. Nevertheless, the generic behaviour of such coupled turbulence-transport cases is already visible in Figure 8: the sharp rise at the edge is due to the nonlinear processes occurring when $V_{Te}/qR > -(c_s \cdot d \ln T_e/d\rho)$, where V_{Te} is the electron thermal velocity. In the core, by contrast, the parallel electron coupling is much more stiff and the nonlinear long-wavelength character of edge turbulence is absent.

CONCLUSIONS

The new modular European Transport Simulator, ETS, developed by the ITM-TF has been applied to simulate the conditions of several JET discharges. The simulations were mostly aiming to module cross-verification and proof of the functionality of workflows coupling, i.e. turbulence code to the transport solver. The ETS workflow was successfully benchmarked against major existing integrated modelling codes [2, 27].

Impurity simulations performed for JET Pulse No: 81856 are capable of reproducing the profiles of radiated power and effective charge in a close agreement with the experiment. They show that the increased radiation during the ICRH phase as compared to the NBI phase may be explained by an increased impurity source at the edge. The increase of the radiation is caused mostly by higher concentration of W in the plasma core, particularly by W^{25}–W^{35} ionization states. Instead, plasma effective charge is mostly due to light ions, eg. Be and Ni. On the contrary to the radiated power profile, flat or slightly peaked in the centre, the effective charge profile is hollow with the maximum at the edge. The sensitivity study shows that a possible reason for the W accumulation during the ICRH phase is an increased concentration of W at the edge. In simulations it was not possible to achieve a necessary increase of the W concentration in the centre through the modification of the convective term of impurity transport, although the effect of a radially shaped convective velocity can not be excluded.

A proof of principle of turbulence-transport coupling was demonstrated with the ETS-GEM coupled simulations. The generic behaviour of turbulence driven transport is observed: a sharp rise at the edge due to nonlinear processes, combined with a relatively moderate transport up to the mid radius, due to stronger parallel electron coupling reducing long-wave contributions.

ACKNOWLEDGMENTS

This work, supported by the European Communities under the contract of Association between EURATOM- CEA, CCFE, IPP, IPPLM, IST, ÖAW, Swiss Confederation, VR, was carried out within the framework of the Task Force on Integrated Tokamak Modelling of the European Fusion Development Agreement. The views and opinions expressed herein do not necessarily reflect those of the European Commission.

REFERENCES

[1]. D.P. Coster, et.al., Plasma Science, IEEE Transactions on, 38(9):2085 -2092, 2010

[2]. D. Kalupin, et al., In Europhysics Conference Abstracts (Proc. of the 38th EPS Conf. on Plasma Physics, Strasbourg France, 2011) P. 4.111, Vol. 35G

[3]. https://kepler-project.org/

[4]. Pereverzev, G.V., YushmanovUSHMANOV, P.N., "ASTRA - Automated System for Transport Analysis in a Tokamak", Report IPP 5/98 (2002).

[5]. A.A.Ivanov et al., 32nd EPS Conf. on Plasma Physics, ECA Vol.29C, P-5.063 (2005)

[6]. W. Zwingmann, et al., 2008, Plasma 2007, AIP Conf. Proc. Vol. 993, 11.

[7]. Huysmans G, Goedbloed J, and Kerner W, 1991, in CP90 Conf. on Comp. Physics Proc, page 371,World Scientific Publ. Co.

[8]. Luetjens H, Bondeson A, Sauter O, 1996, Computer Physics Communications **97**, 219

[9]. Houlberg, W.A., *et al*., Physics of Plasmas **4** (1997) 3230

[10]. Sauter et al, Physics of Plasmas **9**, 5140 (2002)

[11]. L. Garzotti, Proc. 39th EPS Conference on Plasma Physics 2012, P1.004

[12]. S.C. Jardin et al. TSC simulation of ohmic discharges in TFTR – Nuclear Fusion 1993, Vol.**33** p. 371

[13]. Waltz R.E. et al 1997 Phys. Plasmas 7 2482

[14]. J. Weiland, ''Collective Modes in Inhomogeneous Plasma'', Institute of Physics Publishing, Bristol, (2000)

[15]. B Scott, Physics of Plasmas **12** (2005) 102307

[16]. Figini L et al., 2012, EPJ Web of Conferences **32**, 01011

[17]. Schneider R, et al., 2006, Contribution to Plasma Physic **46**, 3, DOI 10.1002/ctpp.200610001

[18]. D. Kalupin et al., In Europhysics Conference Abstracts (Proc. of the 35th EPS Conf. on Plasma Physics, Hersonissos, Crete, 2008), P-5.027, Vol. 32D

[19]. D.Coster, et. al., Journal of LATEX class files, vol. **6**, no. 1, January 2007

[20]. J.F. Artaud, V. Basiuk, F. Imbeaux et al., Nuclear Fusion **50** (2010) 043001

[21]. R. Zagorski, et al., Contribution to Plasma Physics Vol.**52**, No.5-6, 379-383(2012)

[22]. H. P. Summers, (2004) The ADAS User Manual, version 2.6, http://www.adas.ac.uk

[23]. S Wiesen et al, JET ITC-Report 2008

[24]. M.-L. Mayoral, Proc. 24th IAEA Fusion Energy Conference 2012, EX/4-3

[25]. A. Czarnecka et al. Plasma Physics and Controlled Fusion **53** (2011)
[26]. D. Post et al At. Data Nuclear Data Tables **20** (1977) 397
[27]. G. Falchetto et al, *The European Integrated Tokamak Modelling (ITM) effort: achievements and first physics results*, submitted to Nuclear Fusion.

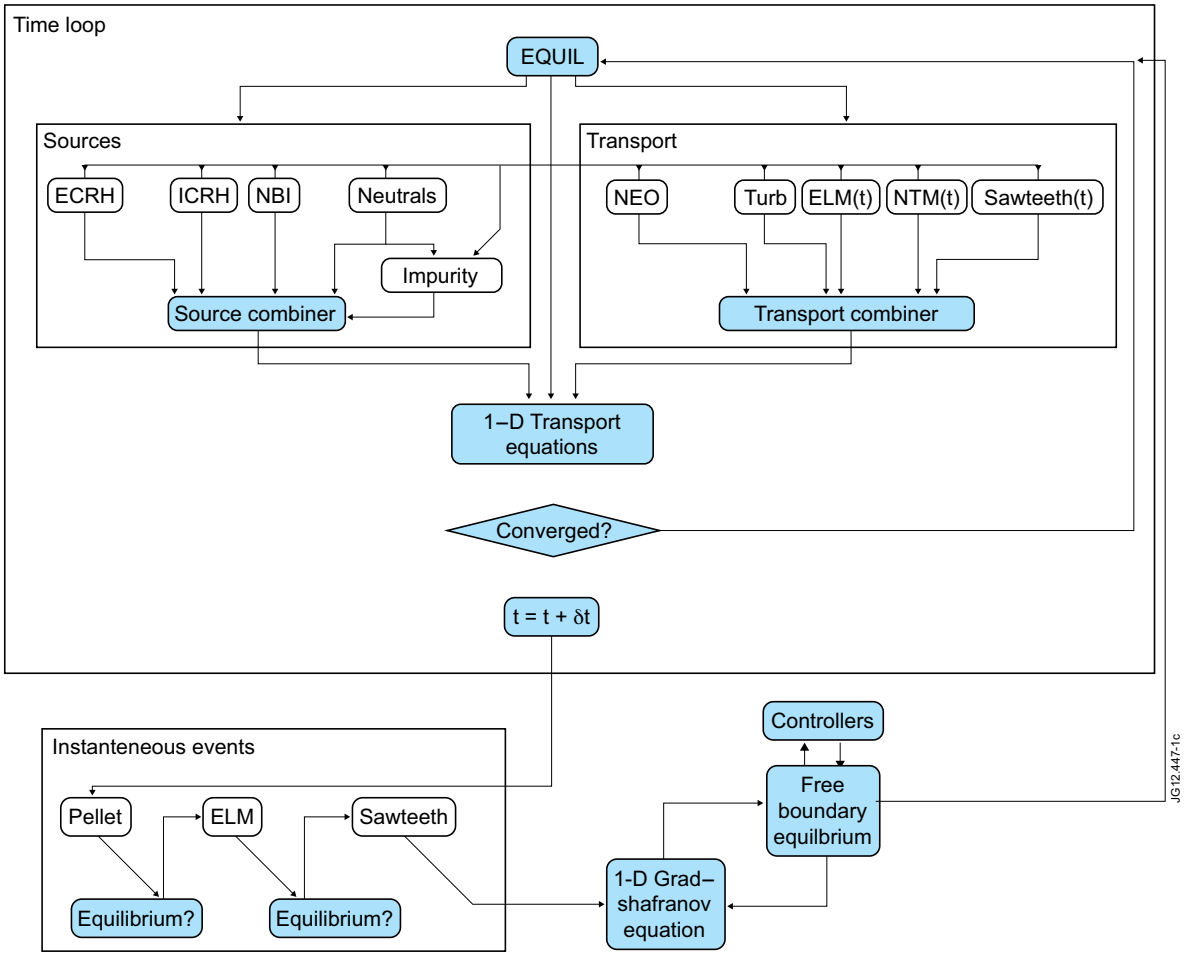

Figure 1: European Transport Solver: a schema of the workflow.

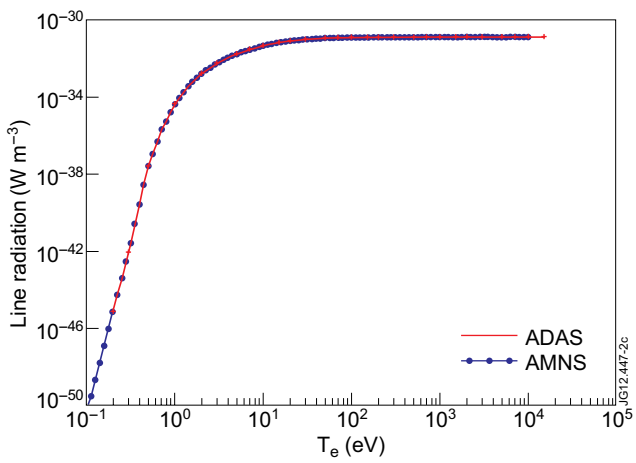

Figure 2: A comparison of the rate coefficient for line radiation for neutral tungsten from the AMNS system with the data from ADAS, for a density of 1×10^{21} [m^{-3}] as a function of electron temperature.

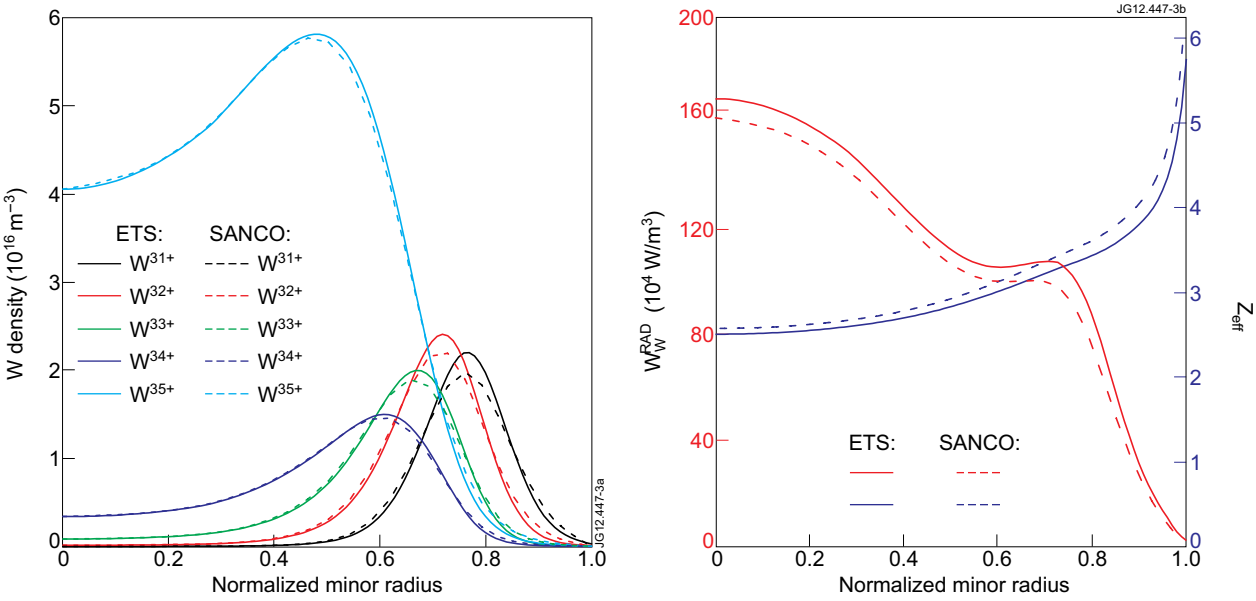

Figure 3: Benchmarking of ETS impurity solver with SANCO code for conditions of JET tokamak assuming parabolic plasma profiles.

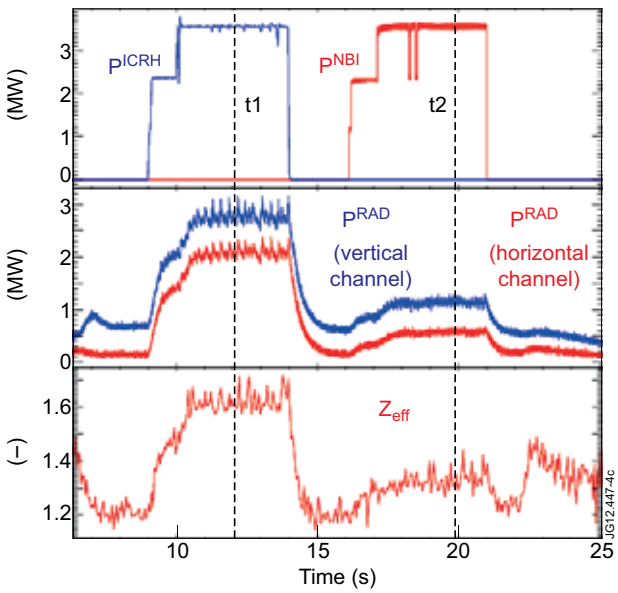

Figure 4: JET Pulse No: 81856. Time traces of auxiliary heating power, radiative losses and line averaged effective charge).

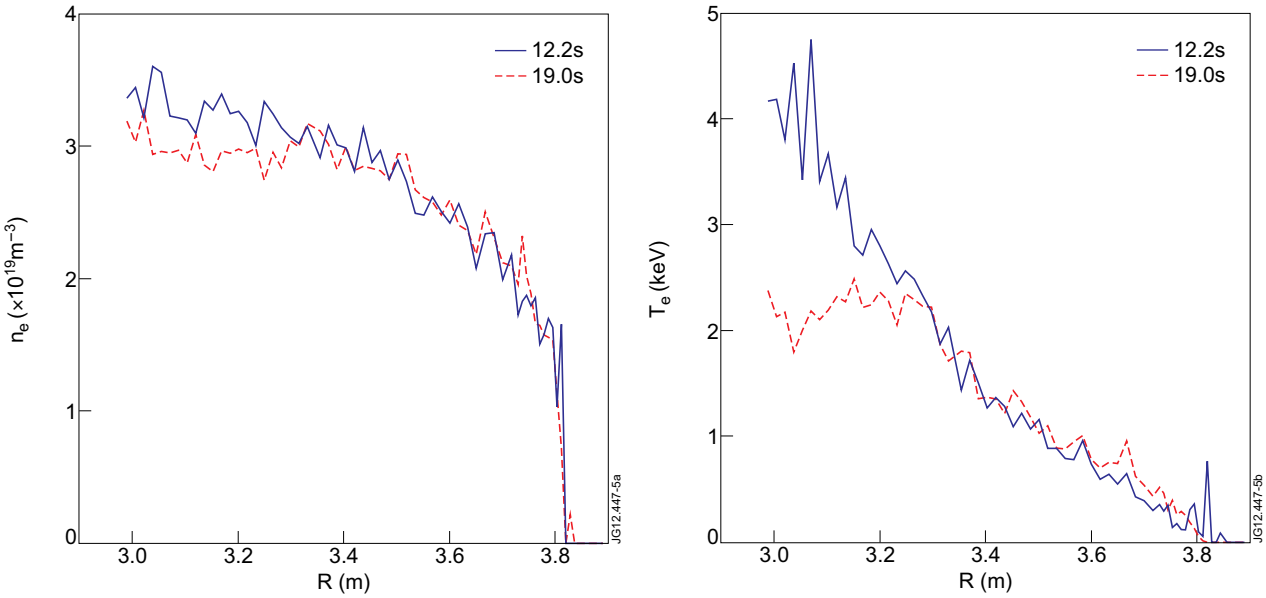

Figure 5: Comparison of experimental profiles of electron density and temperature for ICRH (blue) and NBI (red) heating phases in Pulse No: 81856.

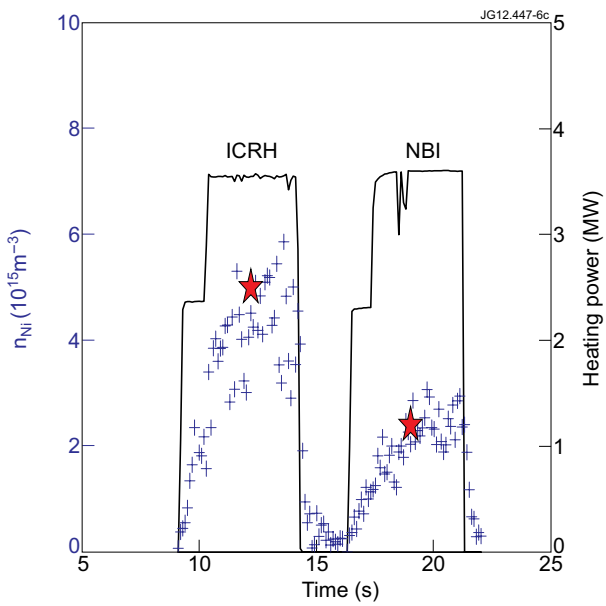

Figure 6: ETS input: Total density of Ni in the Pulse No: 81856 obtained with SPRED diagnostic (blue crosses) and assumed in ETS simulations (red stars).

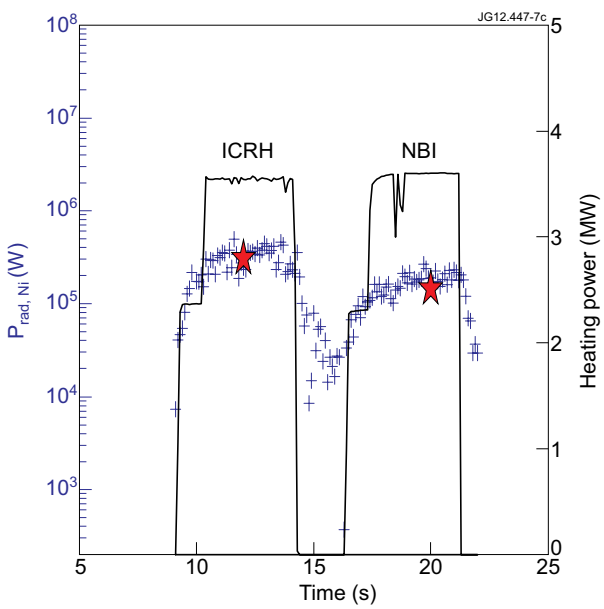

Figure 7: ETS output: Benchmark of radiation (red stars) from Ni obtained with ETS to the one computed from experimental data using UTC code (blue crosses).

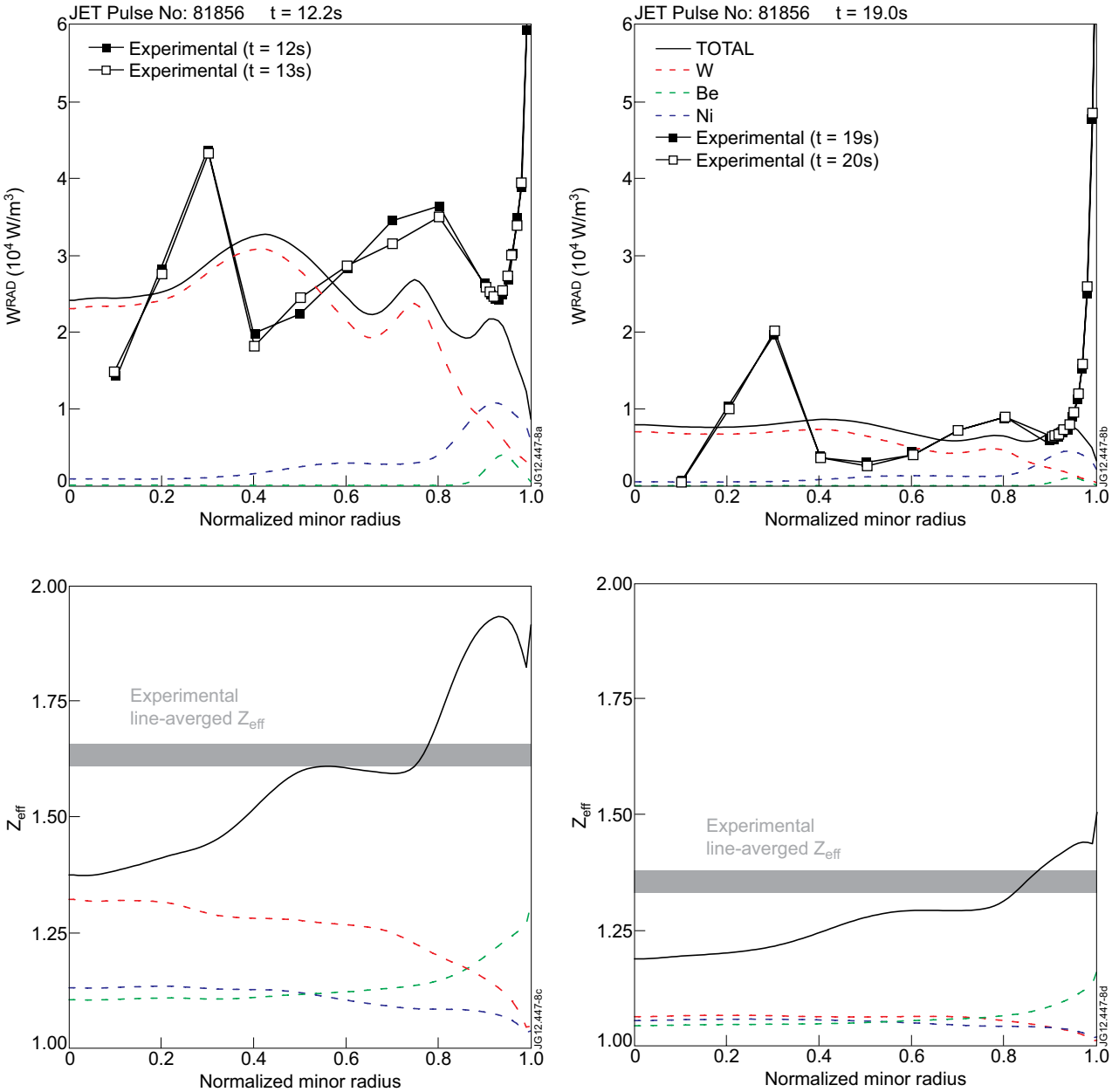

Figure 8: Comparison of simulated steady state profiles of radiative power density and effective charge with experimentally measured ones: black curves – total profiles, red curves – W contribution to the total; blue curves – Ni contribution to the total; green curves – Be contribution to the total.

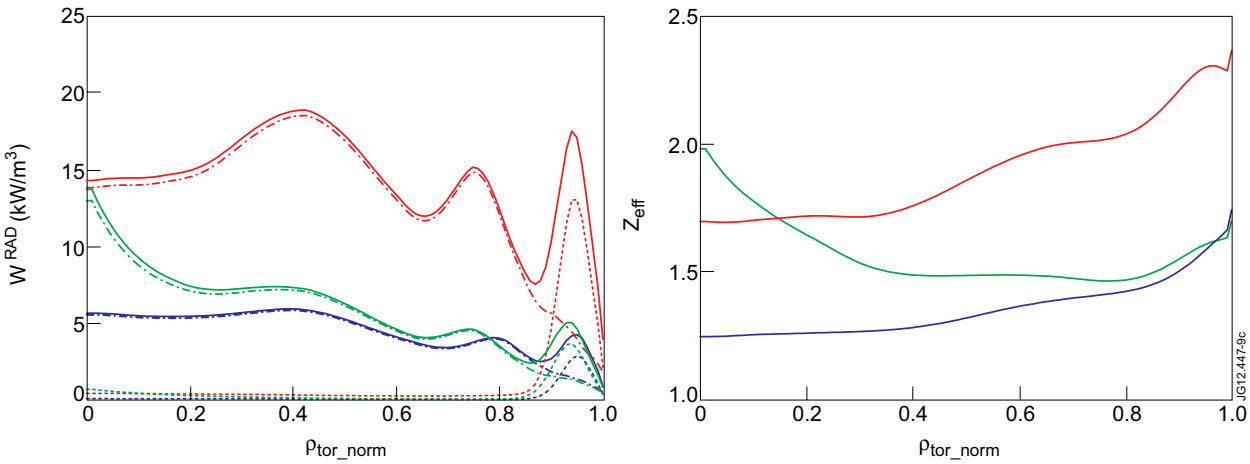

Figure 9: JET Pulse No: 81856. Simulated steady state profiles of radiative power density and Zeff: blue curves – time t2 (reference case;, red curves – time t1 with the assumption of increased source for Be and W; green curves – time t1 with the assumption of increased inward particle pinch for Be and W. Dashed curves – contribution to the radiative loss from all Be ionization states; dash-dot curves – contribution from all W ionization states.

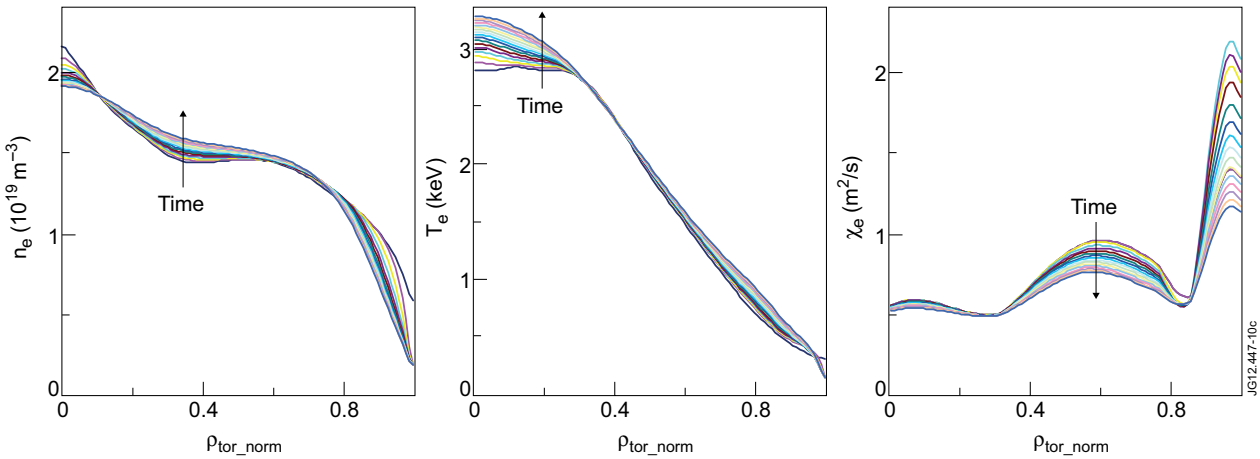

Figure 10: Transport-turbulence coupled computations: relaxation of electron density and temperature profiles (over 15 transport time steps) due to GEM transport coefficients.